

# Detecting neutral hydrogen in emission at redshift $z \simeq 1$

Nishikanta Khandai<sup>1</sup>, Shiv K. Sethi<sup>1,2</sup>, Tiziana Di Matteo<sup>1</sup>, Rupert A.C. Croft<sup>1</sup>, Volker Springel<sup>3,4</sup>, Anirban Jana<sup>5</sup>, Jeffrey P. Gardner<sup>6</sup>

<sup>1</sup> *McWilliams Center for Cosmology, Carnegie Mellon University, 5000 Forbes Avenue, Pittsburgh, PA 15213, USA*

<sup>2</sup> *Raman Research Institute, C. V. Raman Avenue, Sadashivanagar, Bangalore 560080, India*

<sup>3</sup> *Heidelberg Institute for Theoretical Studies, Schloss-Wolfsbrunnengasse 35, 69118 Heidelberg, Germany*

<sup>4</sup> *Zentrum für Astronomie der Universität Heidelberg, Astronomisches Recheninstitut, Mönchhofstr. 12-14, 69120 Heidelberg, Germany*

<sup>5</sup> *Pittsburgh Supercomputing Center, 300 S. Craig Street, Pittsburgh, PA 15213, USA*

<sup>6</sup> *University of Washington, Department of Physics, Seattle, WA 98195-1560, USA*

8 November 2018

## ABSTRACT

We use a large N-body simulation to examine the detectability of HI in emission at redshift  $z \simeq 1$ , and the constraints imposed by current observations on the neutral hydrogen mass function of galaxies at this epoch. We consider three different models for populating dark matter halos with HI, designed to encompass uncertainties at this redshift. These models are consistent with recent observations of the detection of HI in emission at  $z \simeq 0.8$ . Whilst detection of 21 cm emission from individual halos requires extremely long integrations with existing radio interferometers, such as the Giant Meter Radio Telescope (GMRT), we show that the stacked 21 cm signal from a large number of halos can be easily detected. However, the stacking procedure requires accurate redshifts of galaxies. We show that radio observations of the field of the DEEP2 spectroscopic galaxy redshift survey should allow detection of the HI mass function at the  $5\text{--}12\sigma$  level in the mass range  $10^{11.4}h^{-1}M_{\odot} \leq M_{\text{halo}} \leq 10^{12.5}h^{-1}M_{\odot}$ , with a moderate amount of observation time. Assuming a larger noise level that corresponds to an upper bound for the expected noise for the GMRT, the detection significance for the HI mass function is still at the  $1.7\text{--}3\sigma$  level. We find that optically undetected satellite galaxies enhance the HI emission profile of the parent halo, leading to broader wings as well as a higher peak signal in the stacked profile of a large number of halos. We show that it is in principle possible to discern the contribution of undetected satellites to the total HI signal, even though cosmic variance limitation make this challenging for some of our models.

**Key words:** methods: N-Body simulations, cosmology: large scale structure of the universe, galaxies: evolution, radio-lines: galaxies

## 1 INTRODUCTION

Observations show that the cosmic star formation rate (SFR) has declined by more than an order of magnitude since  $z \simeq 1$  (Hopkins 2004). However, a combined census of the cold gas, the fuel for star formation, and stellar components is still largely missing in observations. The cold gas fraction of a halo is a crucial ingredient in models of galaxy formation and constitutes the link to how galaxies obtain gas and subsequently convert it to stars. Hence, measurements of HI in the post-reionization era can place tight constraints on different models of galaxy formation (Putman et al. 2009).

After the epoch of reionization, the neutral hydrogen (HI) survives in dense clouds, e.g. damped Lyman- $\alpha$  systems (DLAs) and Lyman-limit systems (LLS), that are high-redshift equivalents of the HI-rich galaxies that we see at the present epoch. The baryon fraction locked up in HI,  $\Omega_{\text{HI}}$ , in star-forming galaxies in the post-reionization epoch can be determined from the study of damped Lyman- $\alpha$  systems in absorption for  $0.5 \leq z \leq 5$  (Prochaska,

Herbert-Fort, & Wolfe 2005; Rao, Turnshek, & Nestor 2006; Noterdaeme et al. 2009). Even though these observations give clues about aggregate behaviour of star formation as a function of redshift, they cannot be used to infer the total HI mass of these systems because they are seen in absorption. At  $z \simeq 1$ , even the detection of HI in damped Lyman- $\alpha$  has not been easy as the Lyman- $\alpha$  frequency is not accessible to ground-based telescopes. At this redshift, constraints on the global HI fraction come from associated MgII systems, HST observations (for details see Rao, Turnshek, & Nestor 2006, and references therein), and the absorption of 21 cm radiation from bright background radio sources (Kanekar et al. 2009), but with significant uncertainties on the estimated HI fraction. Direct observation of HI in emission and its detailed modelling has only been possible at  $z \simeq 0$  thus far (Zwaan et al. 2005).

Direct observation in 21cm emission of ten massive galaxies have been reported for  $0.17 < z < 0.25$ , with the Arecibo telescope (Catinella et al. 2008). At higher redshifts, the HI emission

arXiv:1012.1880v2 [astro-ph.CO] 14 Dec 2010

from individual clouds is too weak to be detectable with present radio instruments (Bagla, Khandai, & Datta 2010). A long integration time is required for detecting even the brightest objects since the peak signal is a few tens of micro Jansky whereas the system noise is of the order of hundreds of micro Jansky. A possible approach to circumvent the difficulty of detecting individual clouds lies in stacking the HI emission of galaxies with known redshifts. This approach has been attempted for both cluster galaxies and the field galaxies in the recent past (Lah et al. 2007, 2009). In particular, a similar line of study has resulted in the recent detection of HI at  $z \simeq 0.8$  (Chang et al. 2010). An alternative approach rests on the possible detection of the fluctuation in the redshifted HI emission from high redshifts (Bharadwaj & Sethi 2001; Chang et al. 2008; Bharadwaj, Sethi, & Saini 2009).

On the theoretical side, semi-analytical models of galaxy formation have looked at the evolution of cold gas (both in atomic and molecular form) in galaxies and their results match with observations at  $z = 0$  (Obreschkow & Rawlings 2009a; Obreschkow et al. 2009a,b; Obreschkow & Rawlings 2009b; Power, Baugh, & Lacey 2010; Fu et al. 2010; Kim et al. 2010). However observations at higher redshifts are needed to better constrain the evolution of cold gas predicted by these models.

Given the importance of connecting cold gas and stars at  $z \simeq 1$  over a wide range of galaxy environments, it is crucial to make predictions for various detection strategies for current and upcoming telescopes. In this work we focus on the stacking method of individual galaxies with known redshifts to predict how well the HI mass function at  $z = 1$  can be constrained with existing surveys and telescopes (in particular the DEEP2<sup>1</sup> survey and the GMRT<sup>2</sup>; but note that our method is generic and can be extended to future surveys and instruments). By stacking we can also study the contribution of small satellite galaxies, which are undetected in an optical survey but (as we shall show) contain non-negligible amounts of HI, to the total 21 cm signal in emission and also examine the constraints that one can put on the HI mass function.

We model the HI in dark matter halos in a large  $N$ -body simulation by refining the model of Bagla, Khandai, & Datta (2010). Given the paucity of observations at the redshifts under consideration, and our limited understanding of how HI populates dark matter halos at these redshifts, we consider a variety of models. These are constrained by observations of HI at low redshift, simulations of DLAs in small-volumes at high redshift, as well as by some results of semi-analytical models of galaxy formation at intermediate redshifts. In particular, the models that we consider are consistent with recent observations of HI in emission at  $z \simeq 0.8$  (Chang et al. 2010).

Our paper is organised as follows. We present our large dark matter simulation in Section 2, and describe our model for the HI distribution in the simulation along-with specifications of the DEEP2 survey as well as the GMRT in Section 3. We discuss our stacking procedure of individual galaxies and the contribution of undetected satellites to the stacked HI spectra in Section 4. In Section 5, we present our results and discuss the prospects of detection with the GMRT, and the constraints that one can put on the HI mass function. We revisit the issue of undetected satellites and its effect on the HI mass function and discuss whether their presence can be detected. Finally, we present our conclusions in Section 6.

$L_{\text{box}}$ ( $h^{-1}\text{Mpc}$ )	$N_{\text{part}}$	$m_{\text{DM}}$ ( $10^8 h^{-1}M_{\odot}$ )	$\epsilon$ ( $h^{-1}\text{kpc}$ )
400	2448 <sup>3</sup>	3.1	6.5

**Table 1.** Basic simulation parameters for our dark matter run. The columns list the size of the simulation box,  $L_{\text{box}}$ , the number of dark matter particles used in the simulation,  $N_{\text{part}}$ , the mass of a single dark matter particle,  $m_{\text{DM}}$ , and the gravitational softening length,  $\epsilon$ . All length scales are in comoving units.

## 2 N-BODY SIMULATION

We have used P-GADGET, a significantly upgraded version of GADGET2 (Springel 2005) which we are developing for upcoming Petascale supercomputer facilities, for running a large dark matter (DM) simulation in a  $\Lambda$ CDM cosmology. The cosmological parameters used were  $\sigma_8 = 0.8$ ,  $n_s = 0.96$ ,  $\Omega_{\Lambda} = 0.74$ , and  $\Omega_{\text{m}} = 0.26$ . The initial conditions were generated with the Eisenstein and Hu power spectrum at an initial redshift of  $z = 159$ . Table 1 lists the basic simulation parameters: the size of the box  $L_{\text{box}}$ , the number of particles  $N_{\text{part}}$ , the mass of a dark matter particle  $m_{\text{DM}}$  and the softening length  $\epsilon$ . Note for reference, our simulation volume is roughly half that of the Millennium Simulation (Springel et al. 2005) but our mass resolution is about a factor of three better.

The frequency and redshift widths corresponding to  $L_{\text{box}} = 400h^{-1}\text{Mpc}$  at  $z = 1$  are  $\Delta\nu_{\text{box}} = 75.8\text{MHz}$  and  $\Delta z_{\text{box}} = 0.239$ . The high resolution and large volume of our simulation enables us to resolve the smallest groups expected to host HI, as well as to look for effects of cosmic variance on observables like the HI mass function. Furthermore, we are able to resolve subhalos in the larger halos. In fact, we will use the distribution of subhalos in redshift space to make predictions on how these subhalos affect the total HI signal.

We use the SUBFIND code (Springel et al. 2001) to find the subhalo catalogue and to measure properties like central coordinate, peculiar velocity, bound mass, maximum circular velocity and velocity dispersion for every subhalo. Groups of particles are retained as a subhalo when they have at least 20 bound particles, which corresponds to a minimum group mass of  $M_{\text{halo}} = 6.3 \times 10^9 h^{-1}M_{\odot}$ . This mass is slightly larger than the mass of the smallest halo which is capable to host HI, as discussed in Section 3. The largest subhalo in an FOF halo is generally characterised by SUBFIND as the central halo, and the other bound structures as satellites. Since the central halo contains most of the mass of the halo, we will loosely refer to it as the halo, and to the smaller ones in its vicinity as subhalos or satellites, where appropriate.

## 3 MODELLING THE HI DISTRIBUTION

Our knowledge of the HI distribution in the Universe out to  $z \simeq 5$  is derived mainly from QSO absorption spectra, where the gas absorbs in the Lyman- $\alpha$  transition of the hydrogen atom. We know from observations that much of the inter-galactic medium (IGM) is highly ionized and does not contain a significant amount of neutral hydrogen. Instead, most of the neutral hydrogen resides in relatively rare damped Lyman- $\alpha$  systems (Wolfe, Gawiser, & Prochaska 2005). DLAs and other high column density absorption features are believed to arise due to gas within galaxies (Haehnelt, Steinmetz, & Rauch 2000; Gardner et al. 2001). It is possible to make an estimate of the total neutral hydrogen content in DLAs

<sup>1</sup> <http://deep.berkeley.edu>

<sup>2</sup> <http://gmrt.ncra.tifr.res.in>

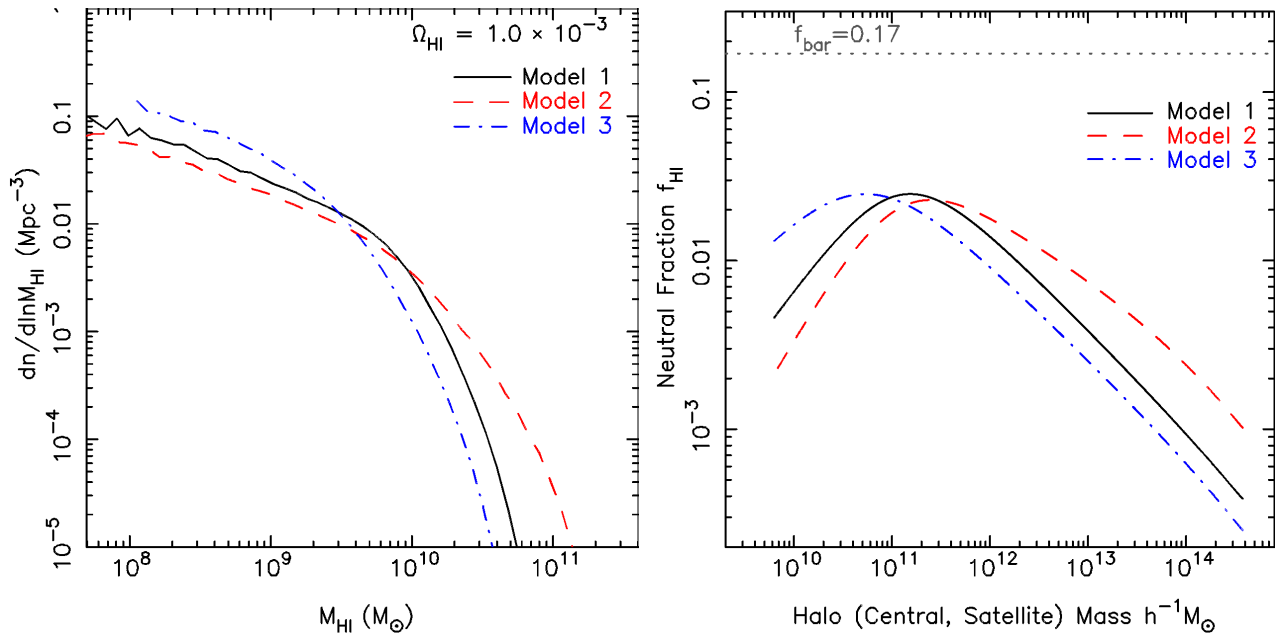


**Figure 1.** *Left:* The mass function for the three models that we consider. Model 1 (solid line) is the Zwaan et al. (2005) mass function but normalised to  $\Omega_{\text{HI}} = 10^{-3}$ . Models 2 (dashed) and 3 (dot-dashed) are variations around Model 1, see Table 2 and Eqn. (2) for details of the model parameters. *Right:* The neutral mass fraction  $f_{\text{HI}} = M_{\text{HI}}/M_{\text{halo}}$  as a function of halo mass for the three models. The (dotted) horizontal line is the baryon mass fraction.

and study the evolution of the total neutral hydrogen content of the Universe (Storrie-Lombardi, McMahon, & Irwin 1996; Rao & Turnshek 2000; Péroux et al. 2005; Prochaska, Herbert-Fort, & Wolfe 2005; Rao, Turnshek, & Nestor 2006; Noterdaeme et al. 2009). Interestingly, these observations suggest that the neutral hydrogen content of the Universe is almost constant in the redshift range  $0.5 \leq z \leq 5$ , with a density parameter of  $\Omega_{\text{HI}} \simeq 0.001$ .

At low redshifts, the HI content can be estimated more directly through emission in the hyperfine transition. Observations of the HIPASS<sup>3</sup> galaxies (Zwaan et al. 2005) in the local universe indicate a much lower neutral hydrogen content ( $\Omega_{\text{HI}}(z=0) \simeq 4.6 \times 10^{-4}$ ) than seen at  $z \geq 1$ . These authors observed HI in emission of  $\simeq 4000$  galaxies in the local Universe to estimate the HI mass function. At higher redshifts, observations in the DEEP2 survey (Gerke et al. 2007) indicate that the fraction  $f_b$  of blue galaxies (generally associated with late type gas-rich galaxies with significant star formation activity) in groups is much higher at redshifts  $0.75 \leq z \leq 1.3$ , increasing from  $f_b = 0.84$  at  $z = 0.75$  to  $f_b = 0.94$  at  $z = 1.3$ , than what is observed in the local Universe. These observations also suggest that  $f_b$  for group and field galaxies approaches the same value by  $z = 1.3$ . We use these observations to motivate our model of assigning HI to dark matter halos at  $z = 1$ .

Here we use the observations of HI in emission at  $z = 0$  (Zwaan et al. 2005) to match the HI mass function to the dark matter halo mass function. We remind the reader that the halo catalogue consists of both centrals and satellites. The Zwaan et al. (2005) HI mass function is given in a Schechter-like form:

$$\Theta(M_{\text{HI}}) = \theta^* \left( \frac{M_{\text{HI}}}{M_{\text{HI}}^*} \right)^{-\alpha} \exp\left(-\frac{M_{\text{HI}}}{M_{\text{HI}}^*}\right) \quad (1)$$

where  $\theta^* = 6 \times 10^{-3} h_{75}^3 \text{Mpc}^{-3}$  is the normalisation factor,

$\log(M_{\text{HI}}^*/M_{\odot}) = 9.8 h_{75}^{-2}$  is the characteristic mass that defines the kink in the function, and  $\alpha = 1.37$  is the slope at the low mass end.  $h_{75} = 0.75$  is the dimensionless Hubble constant. We vary the other models around it.

Marín et al. (2010) took a similar approach to compute the HI bias out to redshifts  $z = 4$ . They also incorporated the fraction of blue galaxies in the local Universe, which is much smaller than what is seen at  $z = 1$  in their model. For this study we take this fraction to be unity. Additionally, we use some input from semi-analytical models and simulations of high-redshift DLAs to motivate our model. Semi-analytical models (Power, Baugh, & Lacey 2010; Kim et al. 2010) suggest that the shape of the HI mass function does not evolve considerably, but shifts toward the high mass end with redshift, assuming a constant molecular to atomic hydrogen ratio,  $\text{H}_2/\text{HI}$ ; though these results may change if this ratio is not a constant (Obreschkow & Rawlings 2009a; Obreschkow et al. 2009a,b; Obreschkow & Rawlings 2009b). This shift may be due to the higher HI content at high redshift, e.g.  $\Omega_{\text{HI}}(z=1) \simeq 10^{-3}$  as compared to  $\Omega_{\text{HI}}(z=0) \simeq 4.6 \times 10^{-4}$ . However, these models do not match the low-end of the Zwaan et al. mass function, due to finite resolution effects of their merger trees.

Hydrodynamic simulations of DLAs at  $z = 3$  by Pontzen et al. (2008) yield a mapping from halo mass to HI mass, which can be described by

$$M_{\text{HI}} \propto \frac{(M_{\text{halo}})^m}{1 + \left(\frac{M_{\text{halo}}}{M_{\text{min}}}\right)^n + \left(\frac{M_{\text{halo}}}{M_{\text{max}}}\right)^p}. \quad (2)$$

These authors found that there is a tight monotonic relation between the virial mass and the HI mass of halos with some scatter. They further found that the  $M_{\text{HI}} - M_{\text{halo}}$  relation has a break at  $M_{\text{halo}}/M_{\odot} \simeq 10^{10.5}$ , suppressing HI in halos larger than this mass and a still stronger suppression in halos with mass  $M_{\text{halo}}/M_{\odot} > 10^{11.0}$ . Furthermore, halos with masses as low as  $M_{\text{halo}}/M_{\odot} \simeq 10^{9.0}$  (or circular velocity at  $z = 3$  of  $v_{\text{circ}} \simeq 30 \text{ km s}^{-1}$ ) are able

<sup>3</sup> HI Parkes All Sky Survey: <http://www.parkes.atnf.csiro.au>

Model	$M_{\min}$ ( $10^{10}h^{-1}M_{\odot}$ )	$M_{\max}$ ( $10^{10}h^{-1}M_{\odot}$ )	m	n	p
1	12	143	1.8	1.36	1.8
2	12	143	2.0	1.36	2.0
3	5	143	1.6	1.15	1.7

**Table 2.** Model Parameters: Mapping of HI mass to halo (centrals and satellites) mass for the three models that we consider. See Eqn. (2) for the functional form of the mapping from HI mass to halo mass.

to host a significant amount of HI. The gas in these halos is able to self-shield from the photo-ionising UV background and maintain a significant amount of HI even though the amount of gas is insufficient for sustaining star formation.

The form of Eq. (2) contains two mass parameters,  $M_{\min}$  and  $M_{\max}$ , for the three regimes in the  $M_{\text{HI}}-M_{\text{halo}}$  relation of Pontzen et al. (2008). Based on their simulations, we choose the cutoff mass for halos not hosting any HI to be  $M \simeq 10^{9.0}h^{-1}M_{\odot}$  or  $v_{\text{circ}} \simeq 30 \text{ km s}^{-1}$  at  $z = 3$ . We use the scaling relation

$$M_{\text{vir}} \simeq 10^{10} M_{\odot} \left( \frac{v_{\text{circ}}}{60 \text{ km s}^{-1}} \right)^3 \left( \frac{1+z}{4} \right)^{-3/2} \quad (3)$$

with  $v_{\text{circ}} = 30 \text{ km s}^{-1}$  to determine the cutoff mass of halos which do not host significant HI. This translates to  $M_{\text{cutoff}}^{\text{halo}}/M_{\odot} = 10^{9.55}$  at  $z = 1$ .

Table 2 summarizes all the parameters for our three models for the HI distribution over halos. Our reference model (model 1) matches the Zwaan et al. mass function but is renormalised to  $\Omega_{\text{HI}}(z = 1) = 10^{-3}$ . We also consider two alternative models around the reference model. In model 2, we allow a larger fraction of HI in large mass halos and suppress HI in lower mass halos. The third model is one in which the HI content in high mass halos is suppressed and the HI is redistributed to lower mass halos. Given our lack of knowledge about how HI populates dark matter halos, these three models should encompass a reasonable range of possibilities. All models are normalised to the fiducial value of  $\Omega_{\text{HI}} = 10^{-3}$ . The form of the mapping from dark matter halo mass,  $M_{\text{halo}}$ , to HI mass,  $M_{\text{HI}}$ , is given in Eq. (2), which is a more generalised form of the mapping considered by Wyithe & Brown (2010). Note that the ratio of the indices  $m$  and  $p$  determines the HI content of halos with mass  $M_{\text{halo}} > M_{\max}$ . In models 2 and 3,  $m/p = 1$ , which means that the HI content in halos larger than  $M_{\max}$  approaches a constant. On the other hand, the value  $m/p < 1$  for model 3 suppresses HI in larger halos.

The model mass functions for all the three models are shown in the left panel of Figure 1. The fiducial mass function (solid line) is the one whose shape matches that of the Zwaan et al. mass function, but is normalised to  $\Omega_{\text{HI}} = 10^{-3}$ . The mass function of model 2 (dashed line) has comparatively more HI in larger halos while the HI in smaller halos is suppressed. On the other hand, the mass function of model 3 (dot-dashed line) suppresses HI in larger halos, with the HI being redistributed to lower mass halos.

In the right-hand panel of Figure 1, we plot the mass fraction of HI ( $f_{\text{HI}} = M_{\text{HI}}/M_{\text{halo}}$ ) as a function of the mass of the host halo. In all three cases, the HI fraction is peaked around halos of mass in the range  $6 \times 10^{10}h^{-1}M_{\odot} < M_{\text{halo}} < 2 \times 10^{11}h^{-1}M_{\odot}$ , and the peak value is 14% of the baryon mass fraction  $f_{\text{bar}} = \Omega_b/\Omega_m = 0.17$ . Lower and higher mass halos have a suppressed HI fraction, which is due to the ratio of slopes ( $m/n$ ) and ( $m/p$ ) being smaller or equal to unity in Eqn. (2). The dependence of the

HI mass on halo mass is again reflected by the three models. At lower halo masses, model 3 has a higher HI fraction followed by model 1 and model 2, however, at the higher mass end the situation is reversed. This is also illustrated in Figure 2, where we show the distribution of dark matter particles at  $z = 1$  in a thin slice through our simulation enclosing the largest halo. The bottom panels zoom-in to a region of dimension  $50 \times 50 \times 4 (h^{-1}\text{Mpc})^3$  centred on the largest halo and showing the HI fraction  $f_{\text{HI}}$  for halos only, for the three models (left to right). As discussed earlier, the smaller mass halos in model 3 have a higher neutral fraction in comparison to the other two models. In all models the largest halos have a smaller neutral fraction, with model 2 dominating over the other two models.

Before proceeding, it is worthwhile to point out the advantages of using a numerical N-body simulation over a halo-model based approach. In the latter, properties like halo (and subhalo) abundances, halo profiles, velocity dispersions and the halo-to-halo scatter are typically calibrated from simulations such as ours (even so often based on much smaller ones). Once appropriate fitting functions are determined, they can be used to predict the signal to a certain accuracy. However, the approach cannot be used to construct a mock map with which the efficiency of signal extracting can be studied. The clustered distribution of halos in a volume is crucial for properly describing the signal. Halos often occupy common pixels in a map and may add in various combinations to the total signal of a given pixel. The noise in a pixel is a fixed random value irrespective of how many halos contribute to the signal in that pixel. Techniques for extracting the signal from a map need to be explored when presenting results for its detectability with instruments. A halo model is generally not able to account for these effects accurately and as a result tends to overpredict the significance of detection. This issue will become clearer when we discuss how the signal is extracted from a mock map for the noise levels that we consider, in Sections 4 and 5.

### 3.1 A Common Field of View for DEEP2 and the GMRT

In this Section, we describe our fiducial choices for volume and halos based on the specifications of the DEEP2 survey and the GMRT. The GMRT is a radio interferometer, consisting of thirty 45 m diameter antennas spread over 25 km. Half of the antennas are spread over a central compact array of diameter 1 km, and the remaining half are spread on 3 arms of length 14 km in a Y-shaped distribution. The longest baseline is 26 km and the shortest 100 m. The GMRT operates on 5 central frequencies (151 MHz, 235 MHz, 325 MHz, 610 MHz, 1420 MHz). For this work our focus is on the 610 MHz frequency which corresponds to a redshift of  $z = 1.3$  for the 21 cm line. The operational redshift at this frequency is  $1.18 \leq z \leq 1.44$ . The angular resolution (corresponding to the largest effective baseline) is 5 arcsecs, this translates to a comoving scale of  $d = 114 h^{-1}\text{Mpc}$ . The system temperature is  $T_{\text{sys}} = 102 \text{ K}$  and the antenna sensitivity  $K = 0.32$ . The GMRT has a full bandwidth of 32 MHz over 256 channels.

The DEEP2 survey is a redshift survey with spectra for  $\simeq 40000$  galaxies in the redshift range  $0.7 \leq z \leq 1.4$ . The survey covers 4 strips of dimensions  $0.5^{\circ} \times 2^{\circ}$  of the sky which corresponds to  $20 \times 80 h^{-1}\text{Mpc}$  (comoving) at  $z = 1$ . The total comoving volume of DEEP2 is  $6 \times 10^6 (h^{-1}\text{Mpc})^3$ . The spectral resolution of DEEP2 is  $\simeq 68 \text{ km s}^{-1}$ , and targets were preselected to a limiting magnitude of  $R = 24.1$ . The DEEP2 spectroscopically targets  $\simeq 60\%$  of the objects that pass the apparent magnitude limit. We hence take the completeness of DEEP2 to be  $\simeq 60\%$ .

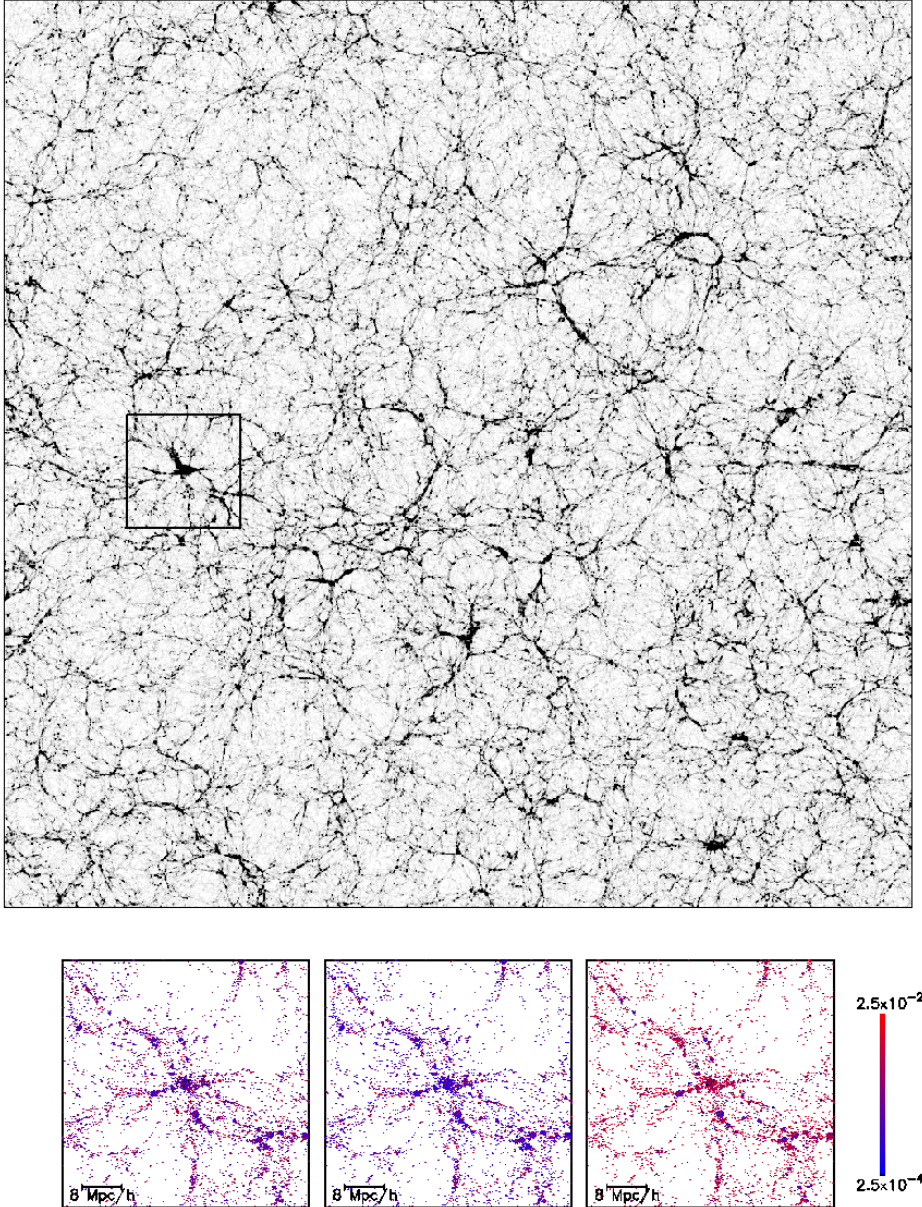


**Figure 2.** *Top:* A thin slice of our simulation enclosing the largest halo (square box), showing the distribution of dark matter particles. *Bottom:* A zoom-in for a region of dimension  $50 \times 50 \times 4 (h^{-1} \text{Mpc})^3$  centred on the largest halo in our simulation, showing the halos which host HI, colour-coded with the neutral fraction  $f_{\text{HI}}$ . The panels from left to right are for the three models.

The overlapping redshift range between DEEP2 and GMRT is  $1.18 \leq z \leq 1.4$ , which corresponds to  $288 h^{-1} \text{Mpc}$  in depth, or nearly a quarter of the DEEP2 volume. Our HI model is at the fixed redshift  $z = 1$  of the simulation output, and not exactly matched to the redshift range of the GMRT, which would require a light cone simulation. Our results should however be a good approximation to redshift averaged quantities such as the mass function. We choose our analysis volume to be of dimension  $50 \times 80 \times 400 (h^{-1} \text{Mpc})^3$ , which is a quarter of the DEEP2 volume. In order to match the required number density of galaxies in DEEP2 (and account for its finite completeness), we choose a minimum threshold mass of  $M > 10^{11.4} h^{-1} M_{\odot}$ . We have compared this threshold to that computed using the known luminosities and estimated mass-to-light ratios for the DEEP2 galaxies (Conroy et al. 2007) and find

good agreement. Above this threshold mass, there are 16388 halos in the subvolume which we identify as galaxies. We also adopt two larger threshold masses for testing our detection strategy; these are  $M > 10^{12.0} h^{-1} M_{\odot}$  and  $M > 10^{12.5} h^{-1} M_{\odot}$ . For these mass cuts there are 3835 and 1031 halos, respectively.

### 3.2 Comparison with Observations

Recently, Chang et al. (2010) reported the first detection of HI in emission from  $z \simeq 0.8$ . They cross-correlated the optical galaxy density field (from DEEP2) with the signal from the redshifted HI line using the Green Bank Telescope (GBT) to obtain a  $4\sigma$  detection. At  $z \simeq 0.8$ , the GBT's angular resolution corresponds to a FWHM of  $9 h^{-1} \text{Mpc}$  (comoving), but the frequency resolution

$\simeq 2 h^{-1}$  Mpc is much finer. Owing to the much poorer angular resolution, Chang et al. (2010) computed the cross correlation along the line of sight direction.

To make a detailed comparison with these observational results, we convolve our simulation box with the angular and frequency resolution to match the analysis of Chang et al. (2010). We also follow Chang et al. (2010) in assuming pixels of size  $(2 h^{-1} \text{Mpc})^3$ . Note that our density field is at  $z \simeq 1$  whereas the observations are at  $z \simeq 0.8$ . This should not pose a serious problem while comparing results, since the only quantity which changes is the mass function of halos and this variation can be absorbed within the models that we consider. We first compute the fluctuating component of both the HI and the galaxy density field on a pixel of size  $(2 h^{-1} \text{Mpc})^3$ . We then convolve these two fields with GBT's point spread function, modelled as a Gaussian with FWHM of  $9 h^{-1} \text{Mpc}$  in the transverse direction and a top-hat of width  $2 h^{-1} \text{Mpc}$  in the redshift direction.

In order to mimic the optical-HI observations, we only assign halos with  $M > 10^{11.4} h^{-1} M_\odot$  in the volume while constructing the galaxy density field. We do not use such a threshold when constructing the HI density field. The cross-correlation as a function of relative displacement,  $r_z$ , along the line-of-sight direction, can be expressed as (Chang et al. 2010):

$$\begin{aligned} \xi_{\text{HI,opt}}(r_z) &= \langle \Delta T_b(d+r_z) \delta_{\text{opt}}(d) \rangle \\ &= 284 \mu\text{K} \langle \delta_{\text{HI}}(d+r_z) \delta_{\text{opt}}(d) \rangle \left( \frac{\Omega_{\text{HI}}}{10^{-3}} \right) \left( \frac{h}{0.72} \right) \\ &\times \left( \frac{\Omega_m + (1+z)^{-3} \Omega_\Lambda}{0.37} \right)^{-0.5} \left( \frac{1+z}{1.8} \right)^{0.5}. \end{aligned} \quad (4)$$

Here  $T_b = 284 \mu\text{K}$  is the 21 cm mean sky brightness temperature,  $\delta_{\text{opt}}$  is the optical density field and  $\delta_{\text{HI}}$  is the neutral hydrogen density field. They are related by  $\delta_{\text{HI}} = br \delta_{\text{opt}}$ , where  $b = \langle \delta_{\text{HI}}^2 \rangle^{1/2} / \langle \delta_{\text{opt}}^2 \rangle^{1/2}$  is the bias and  $r = \langle \delta_{\text{HI}} \delta_{\text{opt}} \rangle / (\langle \delta_{\text{HI}}^2 \rangle \langle \delta_{\text{opt}}^2 \rangle)^{1/2}$  is the stochasticity. By construction  $|r| \leq 1$ . Inserting this into Eqn. (4), one can see that the amplitude of the cross correlation function determines the degenerate combination  $br \Omega_{\text{HI}}$ . Chang et al. (2010) put a constraint on this combination of parameters, obtaining  $br \Omega_{\text{HI}} = (5.5 \pm 1.5) \times 10^{-4}$ . In our simulation we can break this degeneracy. Note that  $r$  and  $b$  are both dimensionless and do not depend on  $\Omega_{\text{HI}}$ . We find for the three models  $b = (0.578, 0.641, 0.538)$  and  $r = (0.923, 0.945, 0.916)$ , respectively. Using the smallest value of  $rb$ , we obtain a constraint on  $\Omega_{\text{HI}}$  of the form  $\Omega_{\text{HI}} = (1.16 \pm 0.30) \times 10^{-3}$ , which is consistent with the value of  $\Omega_{\text{HI}} = 10^{-3}$  taken in our study.

Chang et al. (2010) also computed the cross-correlation along the line of sight direction and normalised it by  $\langle \delta_{\text{opt}}^2(0) \rangle$ . We plot the normalised cross-correlation function in Figure 3 for the three models (solid, dashed and dot-dashed) and compare with the observations of Chang et al. (2010). We find that all the three models are consistent with the observations. Note that model 2 is the most biased of the three models, followed by models 1 and 3. This is expected since the largest halos have a considerably larger HI fraction in model 2, and the largest halos cluster more strongly at smaller scales. A suppression of HI in the largest halos will translate to a lower small-scale bias. The large scale bias is further discussed in the following section.

### 3.3 Finite Volume Effects on $\Omega_{\text{HI}}$

In Figure 4, we look at finite volume effects in the estimation of  $\Omega_{\text{HI}}$ . The size of the subvolume is chosen so as to match the over-

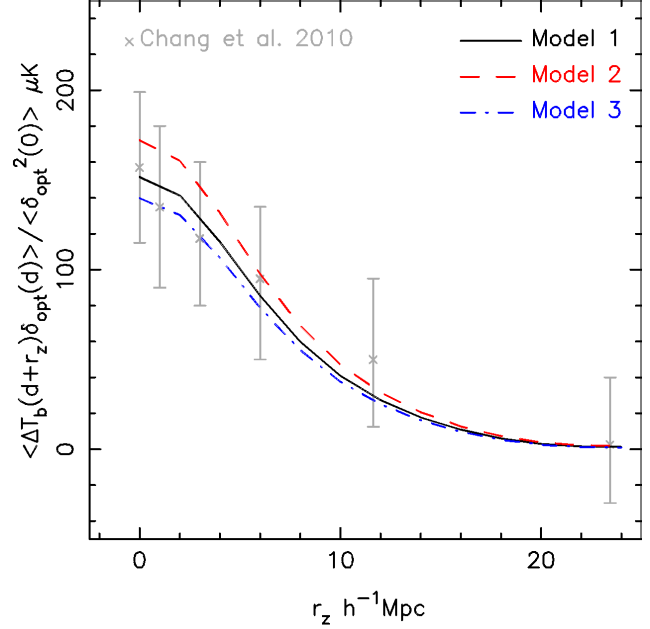


**Figure 3.** Normalised cross-correlation function of the DEEP2 optical galaxy density field and the HI intensity field along the line-of-sight direction (Chang et al. 2010) (data points), and the models 1 (solid line), 2 (dashed line) and 3 (dot-dashed line) that we consider. Note that the cross-correlation function is normalised by the zero-lag auto-correlation function  $\delta_{\text{opt}}^2(0)$  of the DEEP2 optical galaxy density field.

lapping fields of DEEP2 and the GMRT. In our full simulation volume we have 40 such subvolumes. We look at the variations in HI mass in a subvolume with respect to the average HI mass in the entire volume for the three models. These variations are shown for all three models in figure 4 with the same line styles as in Fig. 1. We also plot the variation in  $\Omega_{\text{DM}}^{\text{halo}}$  (dotted line). The rms fluctuation in  $\Omega_{\text{HI}}$  for the three models is  $\simeq 6.8\%$ ,  $7.6\%$  and  $6.2\%$  respectively, whereas the rms fluctuation in  $\Omega_{\text{DM}}^{\text{halo}}$  is  $8.9\%$ . Given that the neutral mass fraction is not uniform but rather peaked around halo masses in the range of  $6 \times 10^{10} h^{-1} M_\odot < M_{\text{halo}} < 2 \times 10^{11} h^{-1} M_\odot$  and suppressed for larger and smaller masses (Fig. 1), the dark matter halos are more strongly biased than HI. This is consistent with Bagla, Khandai, & Datta (2010) who showed that the large scale HI bias increases with a higher neutral fraction in larger halos. Indeed we see that the fluctuation in  $\Omega_{\text{HI}}$  in model 2, which has more HI in larger halos, is closer to that of dark matter halos than the other two models, with model 3 having the least fluctuations. The final volume for our analysis is picked based on the consideration that it should have the smallest fluctuations in HI mass with respect to the mean for the reference model 1.

## 4 THE 21 CM EMISSION SIGNAL

Since the 21 cm line has much larger wavelength than any optical line, the resolution of a radio image is generally much poorer compared to an image made in the optical. Especially at high redshift, a typical radio observation will be looking at most at a few coarse pixels enclosing the target object rather than resolving it with a large number of finer pixels.

In order to create a simulated radio data cube we create a mesh out of the box with each pixel corresponding to an angular width

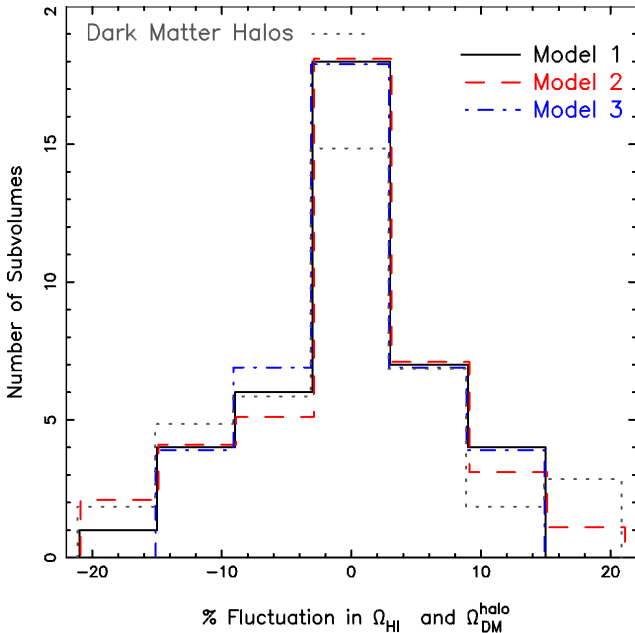


**Figure 4.** Fluctuations in  $\Omega_{\text{HI}}$  for the three models for a subvolume of dimension  $50 \times 80 \times 400 (h^{-1} \text{Mpc})^3$  that we consider. We have a total of 40 such subvolumes. The subvolumes considered for computing fluctuations in  $\Omega_{\text{HI}}$  were the same for all three models. The  $1\sigma$  fluctuations for the three models are 6.8%, 7.6% and 6.2% respectively, for dark matter this value is 8.9%.

of  $125 h^{-1} \text{kpc}$  (comoving), and frequency depth of 125 kHz (this is the width per channel of the GMRT for a single pointing and matches the spectral resolution of DEEP2). The angular resolution is chosen to match that corresponding to the largest baseline of the GMRT. The HI mass in every pixel is computed by integrating the HI mass profiles of halos in the pixels they cover, where a Gaussian profile with a width given by the velocity dispersion of the halo is assumed in redshift or frequency space. Since observations are done in redshift space, we have added the line-of-sight component of the peculiar velocity of the halo to its real space line-of-sight  $z$ -coordinate to obtain its redshift space coordinate.

The stacking of halos is done in the following manner. Halos are first sorted according to their mass. We then identify the central pixel of the halo corresponding to its redshift and its centre in the image plane. Given the location of halos as well as their angular and frequency widths, we first select pixels along a line-of-sight (in frequency) and passing through the central pixel. Stacking is done on the central or zero-reference frequency. For every halo  $i$  the frequency range stacked is  $\pm(4 \times \Delta\nu_i)$  around the halo centre. Once stacked pixels are flagged so as to avoid double counting. After this is done for every target halo, we repeat this procedure for lines-of-sight not passing through the centre but neighbouring pixels in cases where the halo is spread across more pixels. Finally, the search for pixels in frequency space is increased in order to stack the wings of the signal.

In case two target halos whose centres lie within the same line-of-sight are overlapping within  $\pm(4 \times \Delta\nu)$  of each other, parts of the smaller target halo may appear on the wings of the stacked spectra. However, the order of stacking ensures that two halos along the same line of sight are stacked in an optimal manner. If we had chosen to stack around the first halo with the entire frequency range (corresponding to the box), then the second halo would appear on

the wing of the first halo. We have checked that with a frequency width of the pixel finer than 64 kHz we are able to recover the signal reasonably well with this method, similar to what one would get from just stacking analytically (as in a halo model) the flux,  $S_\nu$ , of selected halos of mass  $M_{\text{HI}}$  located at a luminosity distance  $D_L(z)$  with a line profile  $\phi(\nu)$ :

$$S_\nu = \frac{3}{4} \frac{A_{12} M_{\text{HI}} h \nu}{m_{\text{H}}} \frac{1+z}{4\pi D_L(z)^2} \phi(\Delta\nu) \quad (5)$$

Here  $\nu$  is the redshifted frequency  $\nu = \nu_0/(1+z)$ ,  $A_{12}$  is the Einstein coefficient for spontaneous transition from the upper to the lower level,  $h$  is Planck's constant and  $m_{\text{H}}$  is the mass of the hydrogen atom.  $\phi(\Delta\nu)$  is the line profile which we take to be a Gaussian of width  $\Delta\nu = \nu(\Delta v/c)$ , with  $\Delta v$  being the velocity dispersion of the halo.

#### 4.1 Effect of Subhalos on the HI Signal

The signal computed from a halo catalogue is different to that extracted from a map. The HI content in the pixels enclosing a target object is typically greater than the HI mass of the object since lower mass halos as well as interlopers (due to peculiar velocities) add to the pixel with their own HI mass, thereby increasing the signal. This effect is larger in redshift space. In Figure 5 we look at this effect for all the models and for the three mass cuts of  $M \geq 10^{11.4} h^{-1} M_\odot$  (left),  $M \geq 10^{12.0} h^{-1} M_\odot$  (centre),  $M \geq 10^{12.5} h^{-1} M_\odot$  (right). The average signal (in  $\mu\text{Jy}$ ) per halo is plotted as a function of frequency, the zero-frequency marks the central frequency where we have stacked spectra of individual halos. We compare the signal a mock observation would measure (dashed line) when targeting objects with masses above a threshold mass, with the theoretical or modelled expectation (solid line). The modelled signal was constructed by assigning only those halos above the mass cuts in the data cube. Halos below the threshold mass were not assigned to the data cube. In the mock observation, all halos were assigned to the radio data cube and the spectra were stacked for halos above the threshold mass. The contribution of lower mass halos can be seen in Figure 5 where the plots in the second row are the same as those in the first row, but replotted on log-y scale. This is done so as to better illustrate the difference in the wings of the stacked signal, with and without the subhalos. The average signal decreases with decreasing mass cut since lower mass halos have on average a lower peak signal. There is also scatter in the relationship between halo mass (hence HI mass) and peak signal since both the velocity dispersion and the HI mass determine the shape of the signal.

In the mock spectra we find an enhanced peak and broader wings for all the three mass cuts and models. The enhanced signal being larger for the larger mass cuts. The enhancement is as much as 31% for a mass cut of  $M \geq 10^{12.5} h^{-1} M_\odot$ , decreasing to 9% for a mass cut of  $M \geq 10^{11.4} h^{-1} M_\odot$  in model 3 where there is relatively more HI in lower mass halos. The numbers for model 2 are smallest where the HI mass is dominated by larger mass halos, decreasing from 10% for  $M \geq 10^{12.5} h^{-1} M_\odot$  to 4% for  $M \geq 10^{11.4} h^{-1} M_\odot$ . For model 1, the intermediate model, the contribution of subhalos is 22% for  $M \geq 10^{12.5} h^{-1} M_\odot$  and decreases to 7% for  $M \geq 10^{11.4} h^{-1} M_\odot$ .

The larger halos have more substructure as well as interlopers in redshift space, both of which lead to an enhanced signal. To illustrate this point we pick one of the larger halos in the data cube and compute the signal from the pixels that it covers. This is is

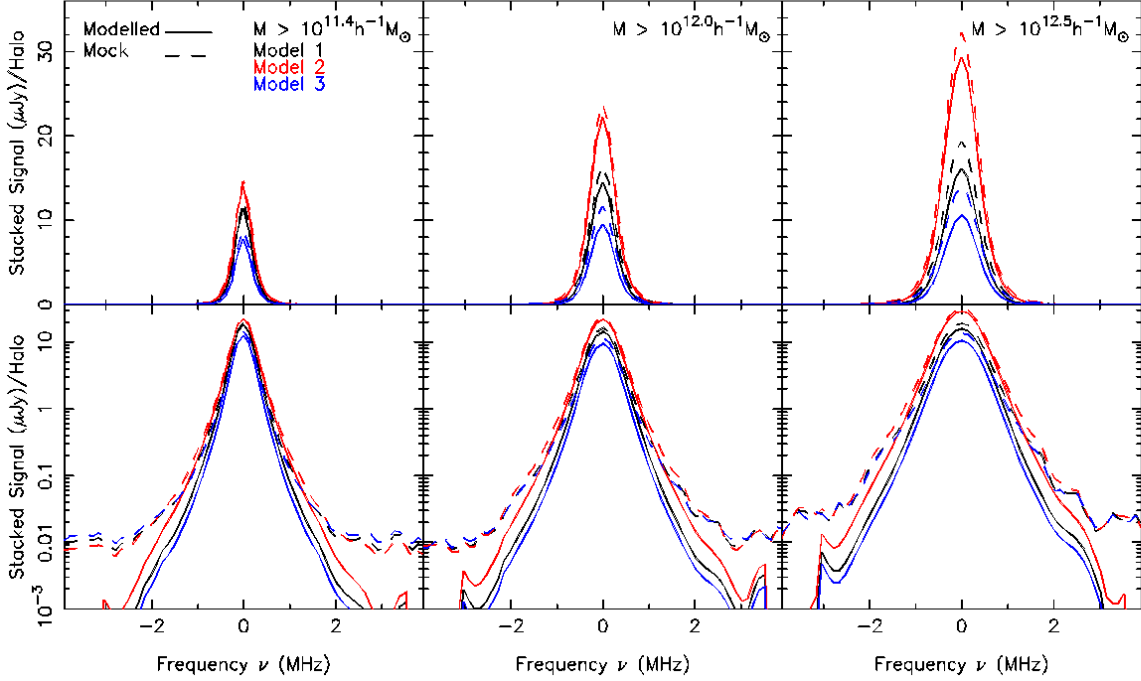


**Figure 5.** The modelled HI emission signal per halo (solid) and the mock signal (dashed), recovered from the radio data cube by stacking, for the three mass cuts  $M \geq 10^{11.4} h^{-1} M_{\odot}$  (left),  $M \geq 10^{12.0} h^{-1} M_{\odot}$  (centre),  $M \geq 10^{12.5} h^{-1} M_{\odot}$  (right). The excess signal in the mock data is due to halos and subhalos below the mass thresholds, which were not identified for stacking. The second row is the same as the first but replotted on a logarithmic  $y$ -axis to better illustrate the broader wings due to subhalos.

shown in Figure 6 for the three models (left to right). This particular halo has a mass of  $M = 2 \times 10^{14} h^{-1} M_{\odot}$ . The black solid line is the (theory) spectrum of the large halo. The blue data points are the theoretical spectra computed from Eqn. (5) of all subhalos within the pixels covered by the large halo, the height and error-bar being the peak signal and its width. These subhalos are below the mass threshold  $M < 10^{11.4} h^{-1} M_{\odot}$  and will not be identified in an optical survey. An observation would see the emission (blue solid line) in excess of the expected signal (black solid line) due to these subhalos. This excess can be as much as 50% of the total signal in model 3, 13% in model 2 and 35% in model 1. The red data points are larger halos, also within the pixels covered by the targeted halo, which are above the minimum mass threshold and would be identified in the optical survey. If these were not separately picked for stacking then we would get an even larger signal (red dot-dashed line). The enhanced signal due to subhalos is within a  $2\Delta\nu$  width of the large halo. If one were to resolve all subhalos and stack them in this case then one would get a peak signal in excess of  $\simeq 140 \mu\text{Jy}$  across models; instead since these are unresolved within the pixel width and are spread across the parent halo we get a peak signal in the range of  $\simeq 22\text{--}55 \mu\text{Jy}$  across models. This effect will show up when we constrain the HI mass function from the signal in a later section and will boost the HI mass of the targeted halo.

One limitation of our model is that we assign an equal amount of HI to both satellite and distinct field halos of the same mass. It is known that gas is stripped from a halo when it merges into a larger halo. Our models hold if an equal fraction of cold gas and dark matter is stripped from a halo during a merger. Conroy, Wechsler, & Kravtsov (2006) argue that the mass of a halo at the time of a

merger,  $M_{\text{infall}}$  is a better predictor of stellar mass (hence luminosity) than the mass of the halo,  $M_{\text{obs}}$  when it is already a satellite. By doing an abundance matching of the luminosity function to the halo mass function with their new definition of mass for satellites, their model reproduces luminosity-dependant clustering of galaxies seen in observations. However their new definition of mass of a satellite seems to affect results more strongly at  $z = 0$  than at  $z = 1$  or higher. If we assume cold gas to trace stars and be more concentrated in the centre of the halo, then based on the results of Conroy, Wechsler, & Kravtsov (2006) at  $z = 1$ , our model should not be sensitive to the environment of small halos. However if cold gas is not concentrated in the centre of halos and is largely stripped during a merger then our model may overpredict the contribution of undetected satellites to the total signal of a large halo.

## 5 RESULTS: DETECTING HI IN EMISSION IN THE DEEP2 FIELD WITH THE GMRT

We now focus our attention to detecting HI in emission in the common field of DEEP2 and the GMRT. We start with a discussion of noise in the GMRT and then proceed to recover the stacked HI emission signal by adding noise to the radio data cube.

### 5.1 Noise In Images

The point source (or angular scales smaller than the synthesized beam of the interferometer) sensitivity,  $\sigma_{\text{rms}}$ , for an interferometer is given by (assuming two polarizations) (Thompson, Moran, &



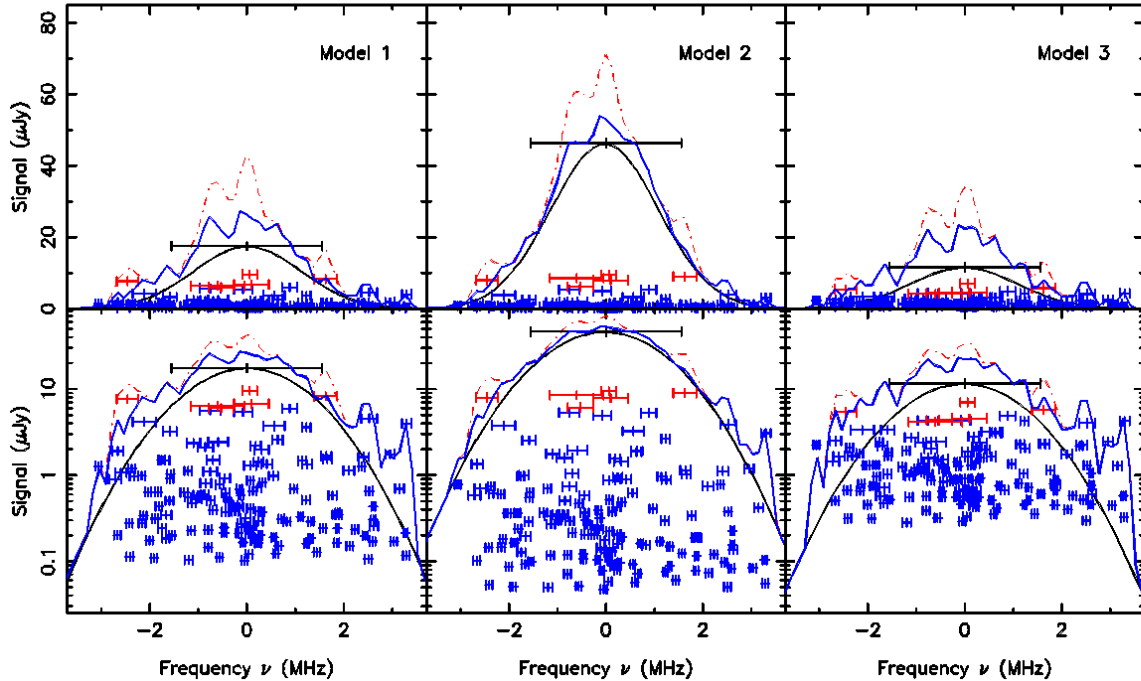


**Figure 6.** Contribution of subhalos and interlopers to the HI signal of a large halo for the three models (left to right). An observation targeting the large halo would see an excess emission signal (blue solid line) compared to the expected (modelled) signal (black solid line) of the large halo. Height and error-bars of each data point denote the peak and width of the theoretical signal of each subhalo or halo. The excess signal is due to subhalos (blue data points) within the pixels of the targeted large halo; these are below the mass threshold of  $M < 10^{11.4} h^{-1} M_{\odot}$  and will not be identified in the optical survey. The red data points are larger halos, also within the pixels covered by the targeted halo, which are above the mass threshold and would be identified in the optical survey. If these were not separately picked for stacking then we would get an even larger signal (red dot-dashed line). This particular halo has a mass of  $M = 2 \times 10^{14} h^{-1} M_{\odot}$ . The second row is the same as the first but replotted on a logarithmic  $y$ -axis to better illustrate the broader wings due to subhalos.

Swenson 2001):

$$\sigma_{\text{rms}} = \frac{T_{\text{sys}}}{K} \frac{1}{\sqrt{\Delta\nu\Delta t\sqrt{2N(N-1)}}}. \quad (6)$$

Where  $K$  (in units of K/Jy) is the antenna sensitivity,  $T_{\text{sys}}$  is the system temperature and  $N$  is the number of antennas,  $\Delta\nu$  is the channel bandwidth and  $\Delta t$  is the integration time. The GMRT has a full bandwidth of 32 MHz with 256 channels, or 125 kHz/channel for the maximum bandwidth in a single pointing. For this bandwidth and  $N = 30$ , the noise per channel is  $\simeq 71 \mu\text{Jy}$  for 24 hours of observation, where  $K = 0.32$  and  $T_{\text{sys}} = 102$  K at the redshifts under consideration.

We need to make several other assumptions to bring the results of our simulation closer to the possible observational outcome. For our stacking approach, we need to co-add signal from sources occupying different pixels in the three-dimensional data cube. However, the noise in neighbouring pixels is not uncorrelated for a radio interferometer; only the noise in different frequency channels is uncorrelated. To take this complication into account, we assume here that the noise is uncorrelated for the spatially separated halos. However for all neighbouring pixels enclosing a target object at a fixed frequency we choose the same noise. To take into account this uncertainty in estimating the noise level and other complications owing to extraction of continuum point sources, etc., we assume two different noise levels:  $\sigma_{\text{rms}} = 420 \mu\text{Jy}$ , which is an estimate of an upper limit, or conservative, noise level on GMRT (see e.g. Lah et al. 2007, for a similar study at a neighbouring frequency), and

$\sigma_{\text{rms}} = 71 \mu\text{Jy}$ , which corresponds to the theoretical (optimistic) noise level computed for 24 hours of observation.

Both noise levels correspond to a pixel of size  $125 h^{-1} \text{kpc} \times 125 h^{-1} \text{kpc}$  (comoving), which is matched to the approximate synthesized beam of GMRT at  $\nu \simeq 700$  MHz, and depth 125 kHz for 24 hours of observation. To every pixel we add a Gaussian random noise with an rms of the two levels of noise that we consider.

## 5.2 Recovering the stacked HI emission spectra

Having added noise to the radio data cube we attempt to recover the stacked emission spectra by doing a  $\chi^2$  analysis. We model the stacked spectra by a Gaussian with three parameters:

$$S_{\text{bf}} = N_{\text{bf}} \exp \left[ - \left( \frac{\nu - \nu_{\text{bf}}}{\Delta\nu_{\text{bf}}} \right)^2 \right] \quad (7)$$

where  $N_{\text{bf}}$ ,  $\nu_{\text{bf}}$ ,  $\Delta\nu_{\text{bf}}$  are the best fit height, centre and width, respectively. We vary these three parameters over a large range and the best fit values are obtained by minimizing  $\chi^2$ . We illustrate this analysis for the fiducial model 1 in Figure 7 for the three mass cuts (columns) discussed earlier and the two noise levels (rows) we consider. For a better illustration of the fits we have changed the scales on the  $y$ -axis for the three mass cuts. Note that this is done for the mock spectra, where all subhalos have been added to the radio data cube. In all cases the reduced  $\chi_{\text{red}}^2 \simeq 1$  which is not a good indicator of the quality of the fit. For the optimistic noise (top row) we

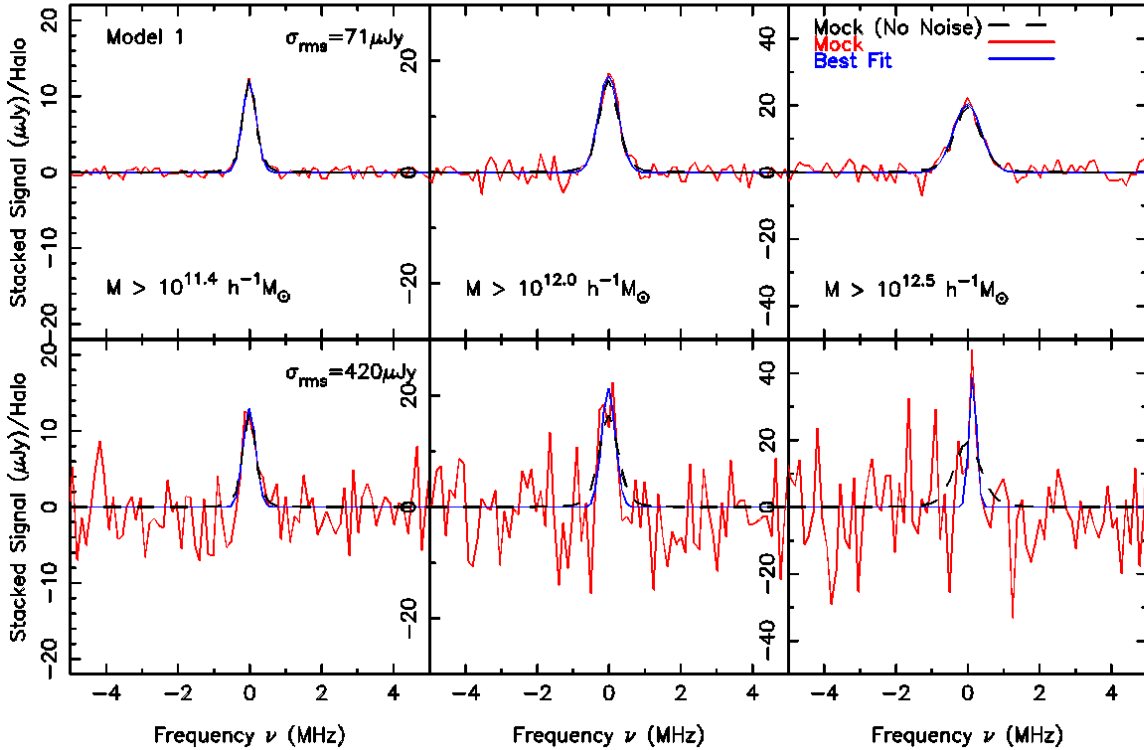


**Figure 7.** Best fit spectra for model 1 by fitting a Gaussian to the mock spectra with rms noise of  $71 \mu\text{Jy}$  (top) and  $420 \mu\text{Jy}$  (bottom), for the three mass cuts  $M \geq 10^{11.4} h^{-1} M_{\odot}$  (left),  $M \geq 10^{12.0} h^{-1} M_{\odot}$  (centre),  $M \geq 10^{12.5} h^{-1} M_{\odot}$  (right). All three fits have  $\chi_{\text{red}}^2 \simeq 1$ .

are able to correctly recover the centre for all the three mass cuts. Visually the best fit (solid blue) seems to match the expected signal (black dashed) extremely well for this case, but note that noise has not been included here. The red line is the mock spectra where noise has been added. For the case of the conservative noise, this is true for a mass cut of  $M > 10^{11.4} h^{-1} M_{\odot}$  where we are able to recover the centre at the zero reference frequency. For a mass cut of  $M > 10^{12.0} h^{-1} M_{\odot}$  the best fit centre is not the zero centre but slightly shifted to the left at  $\nu_{\text{bf}} = 25 \text{ kHz}$ . For a mass cut of  $M > 10^{12.5} h^{-1} M_{\odot}$ , the best fit centre is incorrect and is identified at  $150 \text{ kHz}$ . We also find that the deviation from the expected spectra is the largest for this case, where both the height and the width of the spectra are considerably different than the expected curve. The quality of fits are similar for the other two models.

We now move on to quantify the quality of the recovered spectra by doing a likelihood analysis, where we marginalize over the centre,  $\nu_{\text{bf}}$  and plot the  $1\sigma$ ,  $2\sigma$  and  $3\sigma$  contours for the remaining two parameters, the width  $\Delta\nu_{\text{bf}}$  and the height  $N_{\text{bf}}$  of the stacked spectra. This is shown in Figure 8. The columns represent the models and the rows are for the three mass cuts. The dotted circle is the best-fit value of the width and height. The black contours are for the conservative noise of  $420 \mu\text{Jy}$  and the blue contours are for the optimistic noise of  $71 \mu\text{Jy}$ . The filled diamond is the expected value of the mock spectra without noise, whereas the open square is the same without subhalos. In all cases, the width and height for the spectra without subhalos is smaller than for the ones with subhalos, as was discussed in section 4.1. This is shown again for reference. For both noise levels, we see that the contours are oriented in a manner showing an anti-correlation between height and

width. This is expected since the product of the two determines the mass of the object. This degeneracy which determines the mass of the object is shown in the solid ochre line passing through the expected value of the mock spectra. An incorrect combination of the two would give the same average HI mass per halo.

We find that for the optimistic noise the quality of the fit is extremely good and the best fit values are within  $1\sigma$  of the expected values for the smallest mass threshold of  $M > 10^{11.4} h^{-1} M_{\odot}$  and is within  $3\sigma$  for the other two mass cuts. However, satellites below the threshold mass and contributing to the HI mass of the target halo can be more strongly discriminated with the larger mass cut. The difference being the largest for model 3 and the least for model 2 as discussed in section 4.1. We indeed find that the stacked spectra with and without features of satellite galaxies can be discriminated by more than  $7\sigma$  for the two larger mass cuts and by  $4\sigma$  for the smaller mass cut, in our model. The contribution of satellites in the lowest mass cut corresponds to objects missing in the optical survey.

The GMRT will therefore be sensitive to subhalos that are undetected in the optical survey (although optical stacking would be able to detect them). Inferring what their fractional contribution is could be carried out in various model dependent ways. One can look at specific model predictions (as has been done in this paper) to compare to the stacked signal. One could instead determine how satellite galaxies populate the central halo, i.e. measure the halo occupation distribution, from a different approach. The latter approach should be feasible in a statistical 21cm survey where one observes the 21cm power spectrum (or the correlation function) out to small non-linear scales and infers the HOD from it (Wiythe &

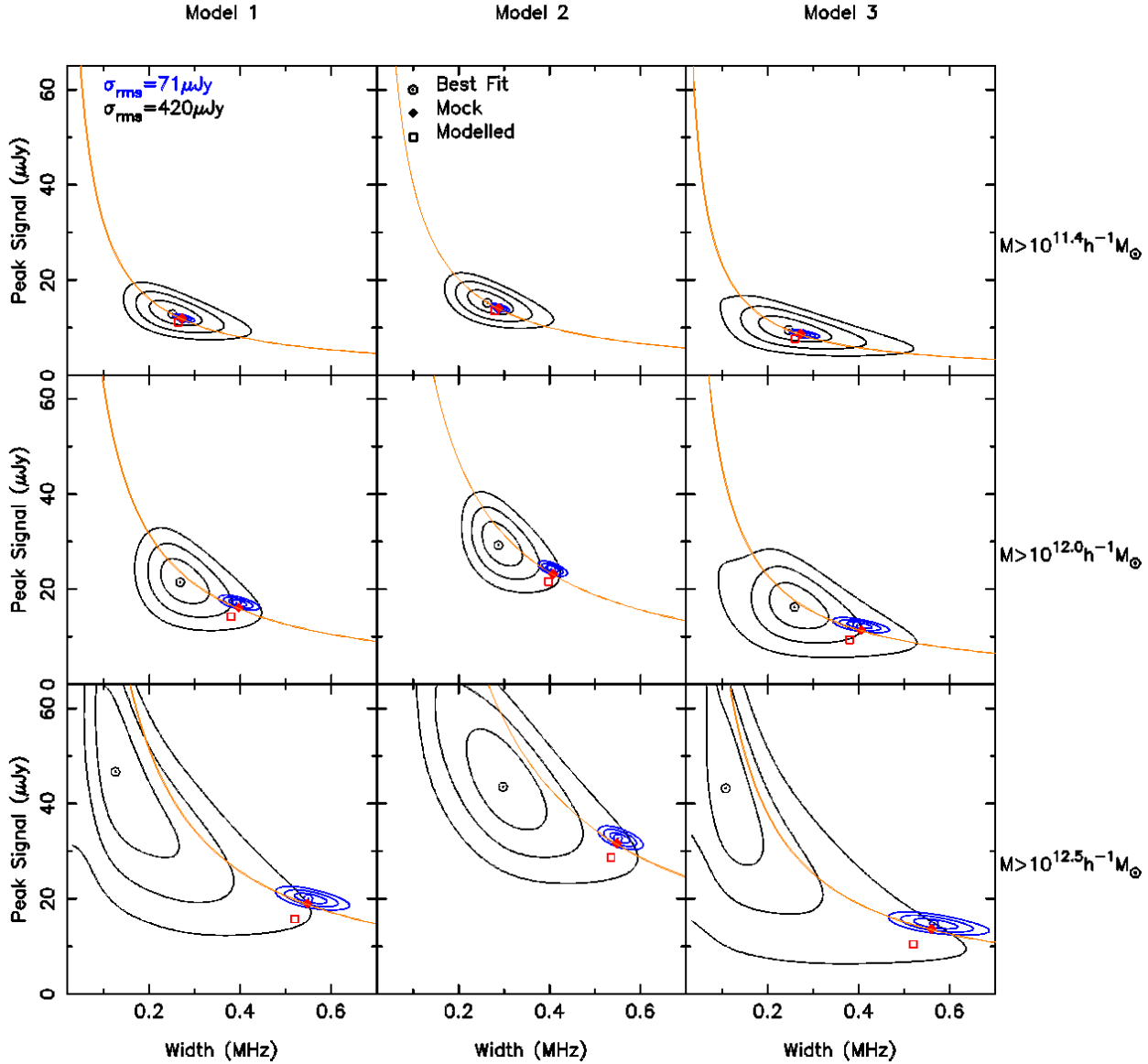


**Figure 8.** Confidence contours for width and height of the fitted Gaussians for the three models (columns) and the three mass cuts  $M \geq 10^{11.4} h^{-1} M_{\odot}$ ,  $M \geq 10^{12.0} h^{-1} M_{\odot}$  and  $M \geq 10^{12.5} h^{-1} M_{\odot}$  (rows). The  $1\sigma$ ,  $2\sigma$  and  $3\sigma$  contours are shown for both the conservative noise of  $420 \mu\text{Jy}$  (black) and for the optimistic noise of  $71 \mu\text{Jy}$  (blue). The dotted circles are the best-fit values from the mock spectra. The open square is the expected point without subhalos, and the diamond is the expected point with subhalos, i.e. mock spectra without noise. The solid ochre line shows the combinations of height and width which give the same mass as the expected average HI mass of the halo from the mock spectra.

Brown 2010). This was done with the correlation function of the HIPASS galaxies at  $z \simeq 0$  (Wyithe et al. 2009). Recently Bagla, Khandai, & Datta (2010) showed that a standalone statistical detection of 21cm clustering would not be feasible with the GMRT or the MWA and will have to wait for future instruments.

For the conservative noise of  $420 \mu\text{Jy}$ , the best fit and the expected value lie within  $1\sigma$  for a mass cut of  $M > 10^{11.4} h^{-1} M_{\odot}$ . This degrades to  $2\sigma$  and  $3\sigma$  for the larger mass cuts. In this case, since the noise is larger, the error-contours are also broader compared to a noise level of  $71 \mu\text{Jy}$ . We also find that the best fit value systematically veers off the line of constant mass in the direction

of lower mass as the threshold mass is increased. This trend is also seen for the lower noise but in the direction of higher mass, but is less prominent. The realisation of noise decides in which direction the best fit value moves when noise becomes important, since it may underpredict or overpredict the HI mass. We cannot distinguish the effect of satellites on the spectra with the conservative noise, unlike the optimistic case. However, as mentioned before, since the best fit value for the two lower mass cuts still lie near the line of constant mass, we would not get the cumulative HI mass wrong, even though the shape of the spectra differs from the true

shape for  $M > 10^{12.5} h^{-1} M_{\odot}$  as seen in the bottom right panel of Figure 7.

The rms fluctuations in the shape of the average spectra when considering all the subvolumes are a few percent and below the fluctuations in total mass. This happens because we fit the average spectra of halos above the mass threshold and not the total spectra. The number of halos above a certain mass cut fluctuates more strongly as an increasing function of this mass cut. Therefore, the effect of cosmic variance is larger in the mass function as compared to the average spectra. We will revisit the issue of cosmic variance on the estimates of the HI mass function in the next section. We do not plot the errors due to cosmic variance in Figure 8 since they are smaller than the size of the symbols.

### 5.3 Subsamples and Constraints on The HI Mass Function

We now discuss the extent to which the HI mass function can be constrained with the GMRT and DEEP2. To obtain the HI mass per halo, or the cumulative HI mass, we need to invert Eqn. (5). We assume a mean redshift  $\bar{z}$  and a mean luminosity distance  $\bar{D}_L$  of our survey, which we take to be at the centre of our subvolume along the redshift direction. The total HI mass is then proportional to the height and the width of the fitted Gaussian and the number of halos above the mass threshold. The error in the HI mass is hence dependent on both: the errors on the height and the width. To obtain the error on either height or width, we further marginalise our likelihood function over the other parameter and compute the  $1\sigma$  errors on them.

We present the constraints on the cumulative HI mass function in Figure 9 for both the optimistic noise of  $71\mu\text{Jy}$  (left) and the conservative noise of  $420\mu\text{Jy}$  (right). The total HI mass for halos above the cutoff mass of the halo has been plotted as a function of cutoff mass of the halo. The uncertainty of the best fit parameters due to noise as well as fluctuations due to cosmic variance have both been included in the error bars, and were added in quadrature. The contribution of each is shown in Table 3. The solid line is the expected cumulative HI mass function and the dashed line is the same without satellites.

The effect of cosmic variance should be more pronounced for rarer or more massive objects. This is indeed the case, as is seen in Table 3, where we find that the fluctuations due to cosmic variance increase with increasing threshold mass for all the three models, the effect being largest for model 2 followed by model 1 and model 3, consistent with the discussion in section 3.3.

In the optimistic case, the mass function can be well constrained over the entire range of masses that we consider. Note that in this case the best-fit points lie systematically above the mock HI mass function, which can be attributed to the noise, as we discussed in the previous section. We had seen in Figure 8 that the contribution of satellites even for the lowest mass cut could be distinguished at the  $3\sigma$  level when we look at the stacked spectra. This is not the case for the mass function, where the cosmic variance is often more dominant than the errors due to noise. We find that the modelled HI mass function is within  $1\sigma$  of the best fit mass function with satellites for model 2 over the entire mass range. This is not so for model 3, where the modelled mass function is well beyond the  $1\sigma$  from the mock mass function over the entire mass range that we consider since the effect of satellites is more pronounced. In model 1, the modelled mass function is within the  $1\sigma$  errors of the mock mass function for  $M > 10^{11.4} h^{-1} M_{\odot}$  and beyond it for the larger mass cuts. From Table 3, we compute the detection significance (including cosmic variance) for the optimistic noise. We find

Errors	Model 1	Model 2	Model 3
$\sigma_{\text{cosm}}(M > M_{11.4})$	8.63%	9.30%	8.59%
$\sigma_{\text{cosm}}(M > M_{12.0})$	10.85%	11.43%	10.87%
$\sigma_{\text{cosm}}(M > M_{12.5})$	13.56%	14.10%	13.58%
$\sigma_{\text{rms}} = 71\mu\text{Jy}$			
$\sigma_{M_{\text{HI}}}(M > M_{11.4})$	6.47%	5.23%	9.37%
$\sigma_{M_{\text{HI}}}(M > M_{12.0})$	8.55%	5.91%	12.11%
$\sigma_{M_{\text{HI}}}(M > M_{12.5})$	11.41%	6.87%	15.34%
$\sigma_{\text{rms}} = 420\mu\text{Jy}$			
$\sigma_{M_{\text{HI}}}(M > M_{11.4})$	42.23%	34.81%	60.04%
$\sigma_{M_{\text{HI}}}(M > M_{12.0})$	40.18%	29.82%	53.62%
$\sigma_{M_{\text{HI}}}(M > M_{12.5})$	108.97%	52.05%	135.63%

**Table 3.** Breakup of errors on the HI mass function due to cosmic variance and noise for models (columns) and the three mass cuts that we consider. The first three rows are the % fluctuations due to cosmic variance for the three mass cuts. Due to lack of space we change the notation of masses, e.g.  $M_{11.4} \equiv 10^{11.4} h^{-1} M_{\odot}$ . The next three (filled) rows are errors in mass estimates due to the optimistic noise of  $71\mu\text{Jy}$  and the final three (filled) rows are for errors in mass estimates for the conservative noise of  $420\mu\text{Jy}$ .

it is the highest for model 2, being  $9.4\sigma$  for  $M > 10^{11.4} h^{-1} M_{\odot}$  and  $11.6\sigma$  for  $M > 10^{12.5} h^{-1} M_{\odot}$ . For models 1 and 3 the numbers are  $(9.3\sigma, 5.6\sigma)$  and  $(7.9\sigma, 4.9\sigma)$  respectively.

We now move on to the case of the conservative noise in the right panel of Figure 9. The best-fit points lie systematically below the mock mass function, in this case, due to the different realisation of noise than in the optimistic case. Here the uncertainties due to noise are much larger than those due to cosmic variance. The modelled HI mass function is well within  $1\sigma$  of the mock mass function, hence the effect of satellites cannot be seen. We find a  $1.7$ – $3\sigma$  detection for mass cuts in the range  $10^{11.4} h^{-1} M_{\odot} < M < 10^{12.0} h^{-1} M_{\odot}$ . A detection is not a possibility for the larger mass cut of  $M > 10^{12.5} h^{-1} M_{\odot}$  for models 1 and 3, whereas a weak detection is possible for model 2 for this mass cut.

## 6 DISCUSSION AND CONCLUSIONS

In this paper, we have studied the prospects for detecting HI in emission at  $z \simeq 1$ . This is a crucial epoch in the study of galaxy formation, since the cosmic star formation rate starts to decline around this time and the missing link in observations is an accurate census of cold gas, which fuels star formation, at these redshifts and beyond (for more discussion of the importance of this issue see e.g. Putman et al. 2009). We make a case that an existing instrument like the GMRT can put strong constraints on the amount of cold gas contained in galaxies, when it is combined with a survey like DEEP2. In this work, we have only focused on the overlapping volume of DEEP2 and GMRT, which represents a quarter of the total DEEP2 volume. Our study is representative of what might be achievable by combining the already existing optical data and the presently operational radio interferometers.

The HI signal is too weak in emission for the detection of individual objects at  $z \simeq 1$ . However, this can be circumvented by a stacking strategy, similar to Lah et al. (2007, 2009), which we

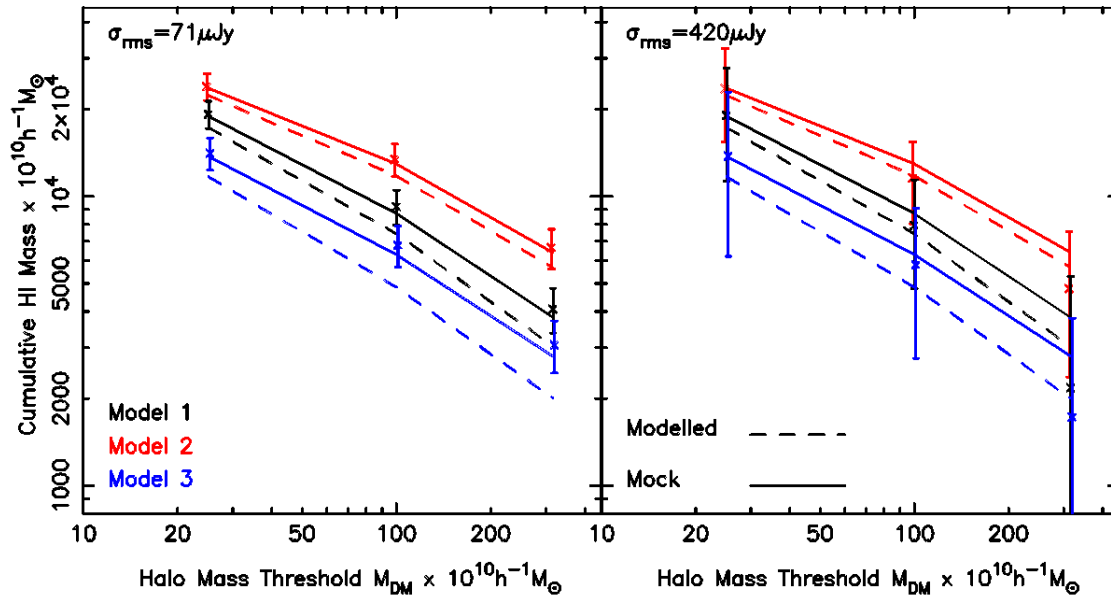


**Figure 9.** The recovered cumulative HI mass function for the three models with the optimistic noise of  $\sigma_{\text{rms}} = 71 \mu\text{Jy}$  (left) and the conservative noise of  $\sigma_{\text{rms}} = 420 \mu\text{Jy}$  (right). The expected mass function with subhalos (solid line) and without subhalos (dashed line) are also drawn for comparison. Data points were computed from the mock spectra.

here apply to look at the prospects of detection. Our conclusions are:

- We find that a detection of HI in emission at redshifts of  $z \simeq 1$  is possible even with existing instruments like the GMRT when combined with the DEEP2 survey. Such an observation will be able to constrain the HI mass function in the halo mass range  $10^{11.4} h^{-1} M_{\odot} \leq M \leq 10^{12.5} h^{-1} M_{\odot}$ . The detection significance is in the range of 5–12 $\sigma$  for an optimistic noise level of 71  $\mu\text{Jy}$  with 24 hours of integration.

- The models that we consider are consistent with recent observations of Chang et al. (2010), who computed the cross-correlation of the density field of DEEP2 galaxies and the 21cm intensity field with the GBT. However these observations allow for all the three models that we consider. On the other hand, we find that using the stacking technique it will be possible to discriminate between the different scenarios with an instrument like the GMRT, at least for the optimistic level of noise.

- Combining our estimates of HI bias with the observations of Chang et al. (2010), we find that the most conservative constraint on the cosmic HI fraction at  $z \simeq 0.8$  to be  $\Omega_{\text{HI}} = (1.16 \pm 0.30) \times 10^{-3}$ .

- We find that undetected satellites in the optical produce a non-negligible contribution to the stacked HI spectra. Their signature is better seen in the stacked spectra rather than in the mass function, since we integrate over one parameter, i.e. the width of the spectra, to obtain the mass function. For a noise of 71  $\mu\text{Jy}$ , features of satellites can be seen at the 4 $\sigma$  level in the stacked spectra for a mass threshold of  $M \geq 10^{11.4} h^{-1} M_{\odot}$ . This detection significance for satellites increases by more than 7 $\sigma$  for  $M \geq 10^{12.0} h^{-1} M_{\odot}$  (see e.g. Fig 8 and Fig. 9). In comparison, the mass function discriminates satellites at the  $\sim 1\sigma$  level.

- We have also considered a much higher level of noise, i.e. 420  $\mu\text{Jy}$ , which should represent an upper bound on noise in the GMRT. With this amount of noise, a detection of the mass function is possible at the 1.7–3 $\sigma$  level. We expect that the real detection sig-

nificance is bracketed by our the optimistic and conservative noise levels.

- For the higher noise, the effect of satellites on the stacked spectra can be seen only at the 1–3 $\sigma$  level across the ranges of mass that we consider. The best-fit parameters of the spectra however are incorrect for the larger mass cuts when compared to the theoretical numbers.

- Cosmic variance affects the mass function more strongly than the average stacked spectra. For this reason, if HI is populated in halos according to model 2 one cannot quantify the effect of subhalos on the mass function due to the effect of cosmic variance. For models 1 and 3, cosmic variance does not swamp the errors due to noise.

One can use the stacking strategy to independently probe  $\Omega_{\text{HI}}$  (Lah et al. 2009). This is not the case in the cross-correlation approach which constrains  $br\Omega_{\text{HI}}$ . As in Lah et al. (2007), it would be useful to also target a subset of galaxies in DEEP2 whose SFR has been measured. This would provide the link between the SFR and the amount of cold gas in galaxies and provide insight into models of galaxy formation. Since spectroscopic surveys are accurate but expensive it would be worthwhile to first try this stacking strategy on future surveys like the LSST, which are designed to give photometric redshifts of  $\simeq 10^{10}$  galaxies. Photometric redshifts are more prone to errors, but it has to be seen if the larger sample of a photo- $z$  survey like LSST could beat down the noise by its sheer number of objects.

In this study, we have modelled the HI in all the halos, centrals and satellites, and we have seen how the satellite population affects the HI mass function as well as the stacked HI profile. The possibility to see the effect of satellites missing in an optical survey in the corresponding 21 cm survey is an exciting prospect. On the one hand, we find that stacking can distinguish between models, but the effect of satellites on the stacked profile is model dependent, and to see their effect one may need to combine it with the cross-correlation approach. In the cross-correlation method the optical density field does not contain all the satellites, whereas the

HI intensity field does. If we use the same mass threshold when constructing the HI intensity field, one naively expects a stronger cross-correlation between the two fields. A preliminary investigation shows that this is indeed the case. We also expect that the HI bias and stochasticity will be sensitive to subhalos. A combination of both approaches would shed light on both the model and the contribution of satellites.

The other approach is to observe the auto-correlation function or the power spectrum of HI, and to constrain the HOD of HI galaxies (Wyithe & Brown 2010) from it. Such an inferred model of HOD when combined with a direct detection as is done here could reveal the contribution of the satellite population on the total signal. We will look into these aspects of the analysis in a forthcoming paper.

Currently operational radio instruments – both single dish and interferometers – have the capability to detect HI in emission at  $z \simeq 1$ , as already demonstrated by Chang et al. (2010). We explored the potential of these complementary strategies. In particular, we studied in detail the efficiency of stacking, possible only with interferometers. In the near future, we expect larger optical galaxy samples at  $z \simeq 1$  and radio observations with wider field-of-views and spectral coverage using upcoming radio instruments (e.g. Johnston et al. 2007). This observational progress will enable a better determination of the HI signal using either of the strategies, thereby substantially improving our estimate of the HI content of galaxies at  $z \simeq 1$ .

## ACKNOWLEDGMENTS

We would like to thank Kevin Bandura and Jeff Peterson for useful discussions on the analysis of their recent paper. We would like to thank Jeffrey A. Newman for useful discussions. This work was supported by NSF award OCI-0749212. This research was supported by an allocation of advanced computing resources provided by the National Science Foundation. The computations were performed on Kraken, Athena, or Nautilus at the National Institute for Computational Sciences (<http://www.nics.tennessee.edu>).

## REFERENCES

- Bagla J. S., Khandai N., Datta K. K., 2010, *MNRAS*, 407, 567  
 Bharadwaj S., Sethi S. K., 2001, *JApA*, 22, 293  
 Bharadwaj S., Sethi S. K., Saini T. D., 2009, *PhRvD*, 79, 083538  
 Catinella B., Haynes M. P., Giovanelli R., Gardner J. P., Connolly A. J., 2008, *ApJ*, 685, L13  
 Chang T.-C., Pen U.-L., Peterson J. B., McDonald P., 2008, *PhRvL*, 100, 091303  
 Chang T.-C., Pen U.-L., Bandura K., Peterson J. B., 2010, *Nature*, 466, 463  
 Conroy C., Wechsler R. H., Kravtsov A. V., 2006, *ApJ*, 647, 201  
 Conroy C., et al., 2007, *ApJ*, 654, 153  
 Gardner J. P., Katz N., Hernquist L., Weinberg D. H., 2001, *ApJ*, 559, 131  
 Gerke B. F., et al., 2007, *MNRAS*, 376, 1425  
 Haehnelt M. G., Steinmetz M., Rauch M., 2000, *ApJ*, 534, 594  
 Hopkins A. M., 2004, *ApJ*, 615, 209  
 Johnston S., et al., 2007, *PASA*, 24, 174  
 Fu J., Guo Q., Kauffmann G., Krumholz M. R., 2010, *MNRAS*, 409, 515  
 Kanekar N., Prochaska J. X., Ellison S. L., Chengalur J. N., 2009, *MNRAS*, 396, 385  
 Kim H.-S., Baugh C. M., Benson A. J., Cole S., Frenk C. S., Lacey C. G., Power C., Schneider M., 2010, arXiv, arXiv:1003.0008  
 Lah P., et al., 2007, *MNRAS*, 376, 1357  
 Lah P., et al., 2009, *MNRAS*, 399, 1447  
 Marín F. A., Gnedin N. Y., Seo H.-J., Vallinotto A., 2010, *ApJ*, 718, 972  
 Noterdaeme P., Petitjean P., Ledoux C., Srianand R., 2009, *A&A*, 505, 1087  
 Obreschkow D., Rawlings S., 2009a, *ApJ*, 696, L129  
 Obreschkow D., Croton D., De Lucia G., Khochfar S., Rawlings S., 2009a, *ApJ*, 698, 1467  
 Obreschkow D., Klöckner H.-R., Heywood I., Levrier F., Rawlings S., 2009b, *ApJ*, 703, 1890  
 Obreschkow D., Rawlings S., 2009b, *MNRAS*, 400, 665  
 Péroux C., Dessauges-Zavadsky M., D’Odorico S., Sun Kim T., McMahon R. G., 2005, *MNRAS*, 363, 479  
 Pontzen A., et al., 2008, *MNRAS*, 390, 1349  
 Power C., Baugh C. M., Lacey C. G., 2010, *MNRAS*, 406, 43  
 Prochaska J. X., Herbert-Fort S., Wolfe A. M., 2005, *ApJ*, 635, 123  
 Putman M. E., et al., 2009, arXiv, arXiv:0902.4717  
 Rao S. M., Turnshek D. A., 2000, *ApJS*, 130, 1  
 Rao S. M., Turnshek D. A., Nestor D. B., 2006, *ApJ*, 636, 610  
 Springel V., White S. D. M., Tormen G., Kauffmann G., 2001, *MNRAS*, 328, 726  
 Springel V., 2005, *MNRAS*, 364, 1105  
 Springel V., et al., 2005, *Natur*, 435, 629  
 Storrie-Lombardi L. J., McMahon R. G., Irwin M. J., 1996, *MNRAS*, 283, L79  
 Thompson A. R., Moran J. M., Swenson G. W., Jr., 2001, *Interferometry and Synthesis in Radio Astronomy, 2nd Edition*, Wiley-Interscience  
 Wolfe A. M., Gawiser E., Prochaska J. X., 2005, *ARA&A*, 43, 861  
 Wyithe J. S. B., Brown M. J. I., 2010, *MNRAS*, 404, 876  
 Wyithe S., Brown M. J. I., Zwaan M. A., Meyer M. J., 2009, arXiv, arXiv:0908.2854  
 Zwaan M. A., Meyer M. J., Staveley-Smith L., Webster R. L., 2005, *MNRAS*, 359, L30